Zhao, J., Lui, H., McLean, D.I., Zeng, H., "Real-Time Raman Spectroscopy for Noninvasive ***in vivo*** Skin Analysis and Diagnosis". In: Recent Advances in Biomedical Engineering, D. Campolo (ed.), pp.455-474, IN-TECH, Vienna, Austria, January 2010.

24

Real-Time Raman Spectroscopy for Noninvasive *in vivo* Skin Analysis and Diagnosis

Jianhua Zhao, Harvey Lui, David I. McLean and Haishan Zeng
Laboratory for Advanced Medical Photonics and Photomedicine Institute, Department of Dermatology and Skin Science, University of British Columbia & Vancouver Coastal Health Research Institute Cancer Imaging Department, British Columbia Cancer Research Center, Vancouver, Canada

1. Introduction

Human skin has been the object of numerous investigations involving noninvasive optical techniques including infrared (IR) spectroscopy and Raman spectroscopy (Zeng *et al.* 1995; Zeng *et al.* 2008; Kollias *et al.* 2002; Richards-Kortum *et al.* 1996; Mahadevan-Jansen *et al.* 1996; Hanlon *et al.* 2000). IR and Raman spectroscopy are complimentary techniques. Both techniques probe the vibrational properties of molecules according to different underlying physical principles. For example, IR spectroscopy is based on the absorption properties of the sample where the signal intensity follows the Beer's Law, while Raman spectroscopy relies on detecting photons that are scattered inelastically by the sample. The intensity of the Raman shift is directly proportional to molecular concentration. The differences in underlying mechanisms confer certain advantages for each method. The instrument for IR spectroscopy is simpler, but the spectra are strongly affected by water absorption in the IR region. The instrumentation for Raman spectroscopy is more complicated than for IR because the Raman signal is extremely weak, but its intensity is proportional to the concentration and independent of the sample thickness. Comparing these two techniques, Raman spectroscopy is more useful for *in vivo* applications. Since its introduction by Williams *et al*. for skin research, Raman spectroscopy has gained increasing popularity (Williams *et al.* 1992; Barry *et al.* 1992). Gniadecka *et al* studied human skin, hair and nail *in vitro* and the signatures of cutaneous Raman spectra have been well documented (Gniadecka *et al.* 1997; Gniadecka *et al.* 1998; Gniadecka *et al.* 2003; Gniadecka *et al.* 2004; Edwards *et al.* 1995). Caspers *et al* reported the Raman properties of different skin layers using *in vivo* confocal microscopy (Caspers *et al.* 1998; Caspers *et al.* 2001; Caspers *et al.* 2003). Raman spectroscopy has also been used to study dysplasia and cancer in a variety of human tissues, including skin (Huang *et al.* 2001a; Huang *et al.* 2005; Huang *et al.* 2006; Gniadecka *et al.* 1997; Gniadecka *et al.* 2004; Lieber *et al.* 2008a; Lieber *et al.* 2008b; Nijssen *et al.* 2002). Because the probability of Raman scattering is exceedingly low it has heretofore been

characterized by weak signals or relatively long acquisition times on the order of several seconds to minutes (Barry *et al.* 1992; Williams *et al.* 1992; Edwards *et al.* 1995; Chrit *et al.* 2005; Gniadecka *et al.* 1997; Gniadecka *et al.* 1998; Gniadecka *et al.* 2003; Gniadecka *et al.* 2004; Shim *et al.* 1997; Nijssen *et al.* 2002). These factors have limited its clinical application in medicine.

The key to implementing Raman in a clinical setting is an integrated system that can provide real-time spectral acquisition and analysis. We are the first to demonstrate the feasibility of real-time *in vivo* Raman spectroscopy for practical clinical applications to the skin by reducing the integration time to less than one second (Huang *et al.* 2001a). Schut *et al.* also reported real-time *in vivo* Raman spectra of the finger, arm, nail, tooth, and tongue using a commercially available probe in combination with software post-processing (Schut *et al.* 2002). Motz *et al* reported a real-time Raman system for studying *in vivo* atherosclerosis (Motz *et al.* 2005a). In this chapter, we detail the design aspects of an integrated real-time Raman spectroscopy system for evaluating the skin. The system includes an image aberration correction feature for full-chip vertical hardware binning, and a software module for real-time data processing. Good signal-to-noise ratio (SNR) Raman spectra can be acquired within one second. This technique can be easily extended to other medical research fields such as lung, cervix or colon cancer diagnosis.

2. Raman Instrumentation

A real-time NIR Raman system is shown schematically in Fig. 1. It consists of five components: light source, light delivery, Raman probe, signal delivery, and signal detection (spectrometer). For real-time Raman spectroscopy, specific design features must be incorporated into each of these components.

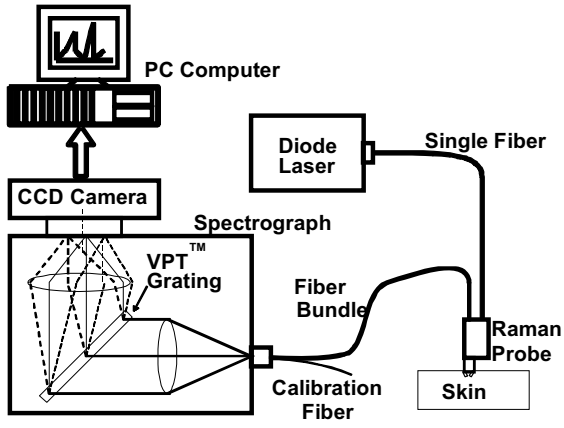

Fig. 1. Block diagrams of the integrated real-time Raman spectrometer system for skin evaluation and diagnosis (Adopted from figure 1a in Zhao *et al.* 2008a with permission).

2.1. Light source

The light sources used in Raman spectroscopy are mainly lasers because of their higher power output and narrower bandwidth. The choice of wavelength for Raman measurement depends on the specific application. For biologic tissue, a NIR laser is commonly used because of its deep penetration depth (700-1100 μm is regarded as the optical window of biological tissues) and the lower level of tissue autofluorescence under NIR excitation. For example, 632 nm, 690 nm, 785 nm, 810nm, 830 nm, and 1064 nm lasers have been reported in *in vivo* and *in vitro* Raman spectroscopy of human tissues (Short *et al.* 2006; Gniadecka *et al.* 1998; Huang *et al.* 2001a; Zhao *et al.* 2008a; Caspers *et al.* 1998; Caspers *et al.* 2001; Caspers *et al.* 2003). Shorter wavelengths are usually used for *ex vivo* thin tissue samples. Both pulsed and continuous-wave lasers are used in Raman spectroscopy. Pulsed lasers are mainly used in time-resolved Raman measurement or time-gated Raman spectroscopy to separate fluorescence from Raman scattering (Morris *et al.* 2005). Ultra-short pulsed lasers can be used in coherent anti-stokes Raman spectroscopy (CARS) (Cheng *et al.* 2004). For conventional Raman spectroscopy, continuous-wave lasers are used most commonly. The critical requirements for the laser source are its intensity and wavelength stability. Solid-state and diode lasers are popular choices for their portability. Our real-time Raman system initially used an external-cavity stabilized diode laser (785 nm, 300 mW, Model 8530, SDL, San Jose, CA) that was subsequently replaced by a solid-state diode laser (785 nm, 350 mW, Model BRM-785-0.35-100-0.22-SMA, B&W Tek Inc., Newark, DE, USA).

2.2. Light delivery

Optical fibers are most commonly used for light delivery in medical applications. The main considerations for choosing optical fibers are numerical aperture, core diameter, core material and its transmission properties. Single mode or polarization-maintaining fibers are rarely used for light delivery in Raman measurement because it is difficult to couple the laser beam into the small core (several microns) of these fibers. Multi-mode 100 – 200 μm core diameter fibers are commonly used. The choice of the numerical apertures (0.22 or 0.37) depends on the collection capability (numerical aperture matching) of the laser system and the lens system. The transmission properties depend on the core and cladding materials. High-OH fibers have high UV and visible wavelength transmission, while low-OH fibers are preferred for NIR and IR wavelength range. Raman signals may arise from the fiber's core material itself and contaminate the tissue signals. Puppels *et al.* studied the Raman properties of a number of commercially-available optical fibers (Santos *et al.* 2005). Choosing the right optical fiber is therefore important for *in vivo* Raman spectroscopy. Our system uses a 200-μm core-diameter low-OH single fiber for laser beam delivery because of its high NIR transmission.

2.3. Raman probe design

Of all the components in biomedical Raman systems, the Raman probe varies significantly according to the specific applications. For endoscopy, Raman probe is entirely composed of fibers because of size limitations. The amount of light delivered to the sample is limited by the thermal hazards. The design of a fiber-based Raman probe is driven by the need to maximize light collection. Because there are huge background signals originating from the laser source, the delivery fibers and other optical components, inline band-pass or long-pass

filters are usually deposited onto the fiber tips to reduce noise, as with the lung (Short *et al.* 2008) and the gastrointestinal (Huang *et al.* 2009) probes. For other applications where size is less critical, specialized lens-and-filter based illumination and collection probes have been designed, such as the graded-indexed GRIN lenses probe (Myrick *et al.* 1990), the compound parabolic concentrator probe (Berger *et al.* 1997), the cervical Raman probe (Mahadevan-Jansen *et al.* 1996) and the ball lens Raman probe (Motz *et al.* 2005b).

The optical layout of our skin Raman probe is schematically shown in figure 2. It is designed to maximize the collection efficiency of the tissue Raman scattering and reduce the interference of the backscattered laser light, fiber fluorescence, and silica Raman signals. It consists of two arms: a 1.27 cm (0.5-inch) diameter illumination arm and a 2.54 cm (1-inch) diameter signal collection arm. In the illumination arm, the laser beam illuminates a 3.5 mm spot on the skin surface at a 40° degree incident angle after having passed through a collimating lens, a band pass filter (785 ± 2.5 nm; Model HQ785/5x, Chroma, Rockingham, VT), and a focusing lens. The band-pass filter can effectively reject Raman scattering and fluorescence that may arise from within the delivery fiber. The laser intensity is controlled so that the surface skin irradiance is 1.56 W/cm², which is lower than the ANSI maximum permissible exposure (MPE) limit of 1.63 W/cm² for a 785-nm laser beam (ANSI Standard Z136.1-1993, American National Standards Institute, Washington, DC) (Huang *et al.* 2001a).

The collection arm has a double-lens (FPX11685/102, JML, Rochester, NY) configuration, with the first lens for signal collection and beam collimation and the second lens for focusing the signal to the fiber bundle. Both lenses have a diameter of 25.4 mm with 90% of clear aperture and an effective focal length of 50 mm, which matches the numerical aperture (N.A.) of the fiber for good throughput. The focal point of the collection lens overlaps the focal point of the illumination lens on the illumination arm. The diameter of the fiber bundle determines the measurement size (1.3 mm on skin surface). In between the two collection lenses lies a high transmission interference 785 nm long pass (LP) filter (LP01-785RU-25, Semrock, Rochester, NY). Because the rejection by the interference LP filter depends on the incident beam angle, two 17.7 mm-aperture windows are used before the LP filter to reject stray light. This arrangement more effectively rejects the laser line and allows us to record Raman shifts down to 500 cm^{-1} for *in vivo* skin tissue.

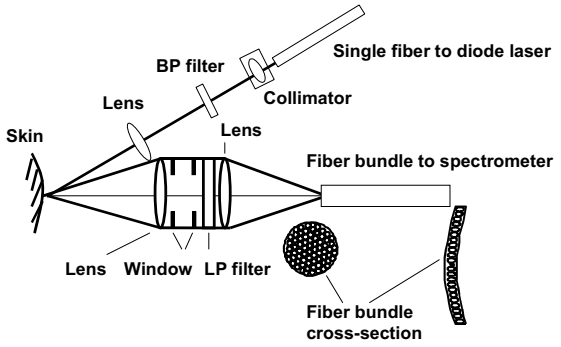

Fig. 2. Block diagrams of the specially designed skin Raman probe. See details in text (Adopted from figure 1b in Zhao *et al.* 2008a with permission).

2.4. Signal delivery

The raw signal, which is composed of Raman scattering and the tissue autofluorescence background, is collected by the probe and transmitted to the spectrometer detection system through a fiber bundle. The fiber bundle is composed of 58 low-OH fibers (100-μm core-diameter). The number of fibers is determined by the height of the CCD detectors (6.9 mm). The distal end of the fiber bundle that connects the Raman probe is packed into a 1.3-mm diameter circular area, which also defines the measurement spot size at the skin surface.

The proximal end of the fiber bundle that is coupled to the spectrograph has a patented design that substantially improves the signal to noise ratio (S/N) of the Raman system (Zeng 2002) and is discussed in detail below under the signal detection section.

2.5. Signal detection

The detection system is equipped with an NIR-optimized back-illumination deep-depletion CCD array (LN/CCD-1024EHRB, Princeton Instruments, Trenton, NJ) and a transmissive imaging spectrograph (HoloSpec-*f*/2.2-NIR, Kaiser, Ann Arbor, MI) with a volume phase technology based holographic grating (HSG-785-LF, Kaiser, Ann Arbor, MI). The CCD has a 16 bit dynamic range and is liquid nitrogen-cooled to -120°C. The *f*-number of the spectrograph (f = 2.2) matches the numerical aperture (N.A. = 0.22) of the fiber, so the throughput is much better than that of a traditional *f*/4 Czerny-Turner spectrographs (Owen *et al.* 1995).

Conventionally the spectrograph is equipped with a straight slit, whose image is well known to be parabolic through a plane grating (HoloSpec, VPT System Operations Manual, Kaiser Optical System, Ann Arbor, MI, 1994). The parabolic shape arises from the fact that rays from different positions along the length of the slit are incident on the grating at varying degrees of obliqueness. For spectrographs with short focal lengths, this obliqueness causes significant distortion that can affect the performance of the detector. For example, the horizontal displacement of a spectral line of our system is shown graphically in figure 3 (Huang *et al.* 2001a), with the displacement rounded to pixels (dashed lines). The maximum horizontal displacement is 5 pixels (135 μm). The solid line is a linear regression-fitted parabolic curve described by $x = 1.1904\times10^{-5}\ y^2 - 1.9455\times10^{-4}\ y - 0.98613$, where x is the horizontal displacement at a vertical position, y. This image aberration causes two problems for hardware binning of CCD detectors: (1) It decreases the spectral resolution and (2) it decreases the S/N ratio. It also causes problems in wavelength calibration. The manufacturer (Kaiser) of the HoloSpec spectrograph suggested a combination of hardware and software binning in which the neighboring pixels along the dashed vertical line are hardware binned, then shifted to the appropriate number of pixels and summing them up with software. As shown in figure 3, there are 11 such hardware-binning groups. Another simple method is a complete software binning procedure, in which the whole image is acquired first and then all the pixels along the curve are added up together using software. However, the improvement of S/N ratio using software binning or combined hardware-software binning is limited because the binning only improves the S/N ratio by as much as the square root of the number of pixels binned together. For signal levels that are readout-noise limited, i.e., weak Raman signal measurements, hardware binning is preferred because it improves the S/N ratio linearly with the number of pixels grouped together. We proposed a simple novel solution for full-chip hardware binning by eliminating this image

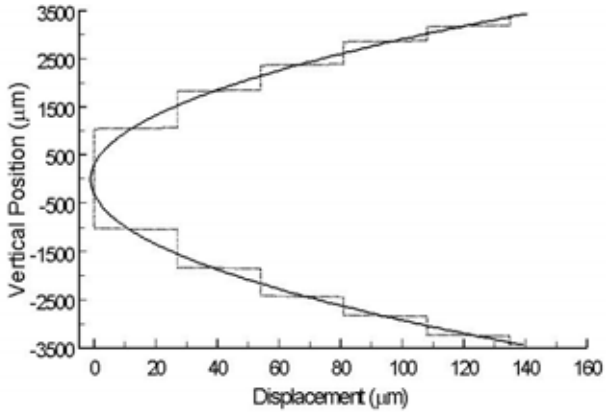

Fig. 3. Graphic representation of the curve observed in horizontal displacement rounded to pixels (dashed lines). The solid curve is a linear-regression-fitted parabolic line (Adopted from figure 3 in Huang *et al.* 2001a with permission).

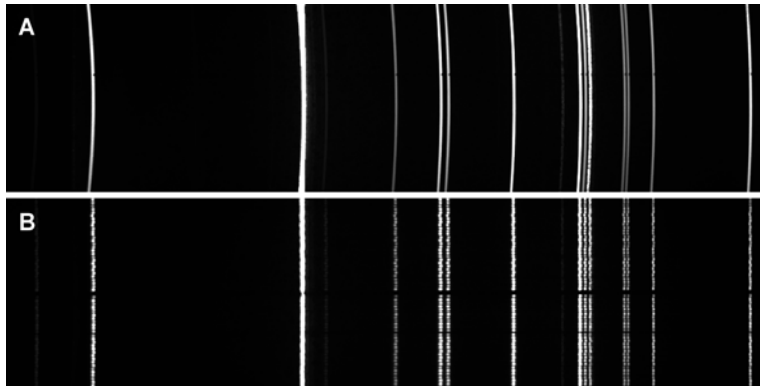

Fig. 4. (a) Mercury-argon lamp image of a 100-μm slit on the CCD through the HoloSpec spectrograph, demonstrating the image aberration. (b) CCD image of 58 fibers aligned along a parabolic line at the entrance of the spectrograph, demonstrating that the image aberration has been corrected (Adopted from figure 2 in Huang *et al.* 2001a with permission).

aberration. As shown in Fig. 2, the 58 fibers of the fiber bundle are aligned at the spectrograph end along a curve formed by the horizontal displacement, but in the reverse orientation. Figure 4a shows the image aberration of a 100-μm slit through the spectrograph in our uncorrected system when it is illuminated by a mercury argon lamp. Figure 4b shows a CCD image of the fiber bundle illuminated by a mercury argon lamp after image aberration correction. The center fiber (dark spot) is used for calibration so that the image of the fibers is symmetrical along the centerline of the CCD detectors. With this specific fiber arrangement the spectral lines are substantially straighter, which enables image-aberration

and full-chip hardware binning along the entire CCD vertical line (256 pixels) without losing resolution and reducing the S/N ratio. The S/N ratio improvement that we achieve with our system is 3.3 times that of the combined hardware and software binning procedure, and 16 times that of the complete software binning (Huang *et al.* 2001a). The spectral resolution of the system with 100-um fiber is 8 cm^{-1}.

3. Software Implementation

The real-time Raman control and data acquisition & analysis system are implemented with Labview (National Instruments, Austin, TX drivers from R Cubed Software, Lawrenceville, NJ) (Zhao *et al.* 2008a). A flow chart of the software implementation is shown in figure 5. The estimate of time cost for each step is marked in millisecond. There are three key steps: system initialization, real-time data acquisition, and real-time data processing.

3.1. Raman system initialization

Before clinical measurement, a number of system calibrations are necessary. These calibrations include wavelength calibration, system spectral response calibration, intensity calibration and CCD dark-noise subtraction. The CCD dark-noise is first measured before each measurement and sequentially subtracted immediately after the CCD readout. Wavelength calibration can be performed using cyclohexane, acetone and barium sulfate, in combination with an Hg-Ar lamp. In our system, 10 major peaks that span the whole wavelength range are used for wavelength calibration. A fifth-order polynomial fitting is used to correlate the CCD pixels with the wavelengths. Because system configuration does not change during the Raman measurement, wavelength calibration can be implemented before the measurement. The spectral response calibration is critical to correct the optical transfer function, which varies from system to system. It is performed using an NIST (National Institute of Standards and Technology) traceable tungsten calibration lamp. The ratios of the known spectral irradiance of the lamp to the measured spectra yield the spectral response correction factors. System-independent spectra are then obtained from the measured spectrum through multiplication by the spectral response correction factors. To facilitate intensity calibration, a NIST traceable reflectance standard disk (SRS-99-020, Labsphere, New Hampshire, USA) was used, which showed stable Raman peaks at 726.56 cm^{-1} and 1379.06 cm^{-1}. The Raman spectrum of the standard disk was measured before each experiment, and then used to correct the intensity variations of the laser beam. The laser output can also be monitored directly for laser intensity correction.

The program starts with system initialization, including the above wavelength calibration, spectral response calibration, intensity calibration and CCD dark-noise subtraction. It also loads all databases or files needed for PCA and LDA analysis as well as the reference Raman spectra for biochemical composition analysis. Other steps are also included such as those necessary for the real time measurement and archiving, setting specific regions of interest (ROI) of the CCD detector, data auto-saving, patient information, and comments etc.

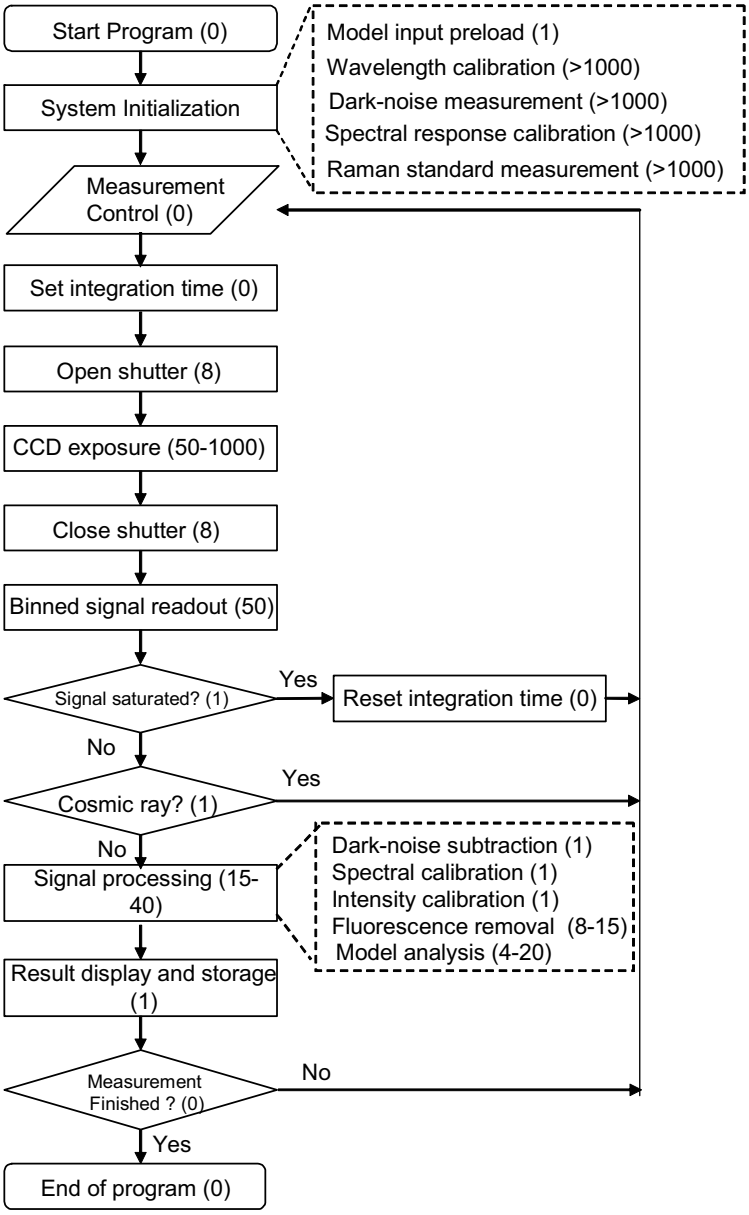

Fig 5. Flow chart of the real-time Raman system. It shows all the necessary steps for processing Raman spectra. The numbers in parentheses are estimates in millisecond (ms) required for each module (Adopted from figure 4 in Zhao *et al.* 2008a with permission).

3.2. Raman data acquisition

After initialization, the system is ready for real-time measurements. Measurements are started via a control signal that can be triggered from the keyboard, hand switch, foot switch, or a signal generated by the program itself. There are two shutters in the system, which essentially have identical response times. One internal shutter lies in the front of the CCD camera to prevent over-exposure or exposure during the readout process. The other lies in the path of laser output to prevent any effect on the skin before measurement, such as photobleaching of tissue autofluorescence (Zeng *et al.* 1998). Both shutters are synchronized to open after the control signal is triggered and then close after a pre-set exposure time. The raw signal (including tissue Raman and autofluorescence background) is read out after the shutter closure.

Both Raman and fluorescence intensities vary according to subject and site within the same subject; for example pigmented lesions exhibit relatively higher NIR autofluorescence (Huang *et al.* 2006; Han *et al.* 2009). The initial choice of integration time may not be optimal. Therefore, signal saturation control is necessary for real-time systems. Signal saturation control can be implemented by reducing the laser intensity as in the atherosclerosis Raman system (Motz *et al.* 2005a), or by reducing the integration time. For our skin Raman measurement, signal saturation control was implemented by reducing the integration time with close to 100% accuracy. Basically we compare the signal with the dynamic range of the CCD detector before background subtraction (i.e. 65535 for a 16-bit dynamic range). To account for noise, any five successive values (except near laser line) of the spectrum beyond the dynamic range will indicate that saturation has occurred. The saturated spectra are then discarded and the data acquisition procedures are repeated automatically with a lower exposure time. The initial integration time is usually set to be equal to or less than 1 second. Experiments show that half of the initial integration time can always suffice for preventing saturation.

Another issue for real-time measurement is cosmic rays, which are detected by the Raman system at an average rate of 1-5% per one-second exposure time. To our knowledge automatic cosmic ray rejection has not yet been incorporated into real-time biomedical Raman systems. Our algorithm for cosmic ray rejection is based on the striking differences between the peak bandwidths of biological tissue Raman peaks which are usually a few tens of pixels, and those of cosmic rays which are usually limited to a couple of pixels. Our algorithm compares each data point with its adjacent 5 points on both sides to determine whether a cosmic ray is present. A sharp peak with bandwidth of only 1-2 pixels will define a cosmic ray signal and prompt the system to repeat the measurement automatically until a cosmic ray-free Raman signal is obtained. For measurements with longer integration times, cosmic rays are unavoidable, and thus, an alternative would be to remove the cosmic ray through software.

3.3. Raman data processing

Real-time data processing includes CCD dark-noise subtraction, spectral response calibration, intensity calibration, fluorescence background removal, and data modeling and analysis (i.e. GLS fitting, PCA, LDA etc). The CCD dark-noise is first subtracted from the cosmic ray-free raw signal before further analysis. After dark-noise subtraction, the spectral response of the system is also corrected using a standard tungsten-halogen lamp, which was

loaded during the system initialization. The laser intensity variation is also corrected. All signals are then scaled to an equivalent integration time of 1 second.

The most important step in real-time Raman spectroscopy is the rejection of NIR autofluorescence background that is superimposed on the Raman signal. The most commonly used method in biomedical Raman measurement is single polynomial curve-fitting (Mahadevan-Jansen *et al.* 1996). As discussed, the major weakness of polynomial fitting is its dependence on the spectral range and the choice of polynomial order (Zhao *et al.* 2007). Lieber *et al* proposed an iterative modified polynomial method to improve the fluorescence background removal (Lieber *et al.* 2003). Recently we proposed the Vancouver Raman Algorithm, which combines peak-removal with a modified polynomial fitting method. This method substantially improves the fluorescence background removal, particularly for spectra with high noise or intense Raman peaks. The advantages of the Vancouver Raman Algorithm are that it not only reduces the computation time, but also suppresses the artificial peaks on both ends of the spectra that may be introduced by other polynomial methods. The algorithm is less dependent on the choice of the polynomial order as well (Zhao *et al.* 2007). A copy of the algorithm for noncommercial use can be downloaded from http://www.bccrc.ca/ci/people_hzeng.html.

A detailed diagram of the Vancouver Raman Algorithm can be found in the reference by Zhao et al. (Zhao *et al.* 2007). It starts from a single polynomial fitting P(ν) using the raw Raman signal O(ν), followed by calculation of its residual R(ν) and its standard deviation DEV, where ν is the Raman shift in cm^{-1}. The quantity of DEV is considered an approximation of the noise level. In order to construct data for the next round of fitting, we compared the original data with the sum of the fitted function and the value of its DEV, defined as SUM. The data set is reconstructed following the rule that if a data point is smaller than its corresponding SUM, it is kept; otherwise it is replaced by its corresponding SUM. Setting DEV=0, is equivalent to Lieber's method (Lieber *et al.* 2003), but applying our rule provides a means for taking into account the noise effect and avoiding artificial peaks that may arise from noise and from both ends of the spectra. In order to minimize the distortion of the polynomial fitting by major Raman signals, the major peaks are identified and are removed from the subsequent rounds of fitting. Peak removal is limited to the first few iterations to prevent unnecessary excessive data rejection. The iterative polynomial fitting procedure is terminated when further iterations cannot significantly improve the fitting, determined by $|(DEV_i - DEV_{i-1})/DEV_i| < 5\%$. As with many iterative computation methods, the percentage can be empirically adjusted by the user according to the problem involved and computation time allowed. However, we recommend it be fixed in the whole process for a given clinical study. The final polynomial fit is regarded as the fluorescence background. The final Raman spectra are derived from the raw spectra by subtracting the final polynomial fit function.

An example of the Vancouver Raman Algorithm and the final Raman spectra is shown in Fig. 6. It is the spectra obtained from solid phase urocanic acid (Sigma Aldrich, USA), which exhibits multiple intense Raman peaks. For comparison purpose, the results for single

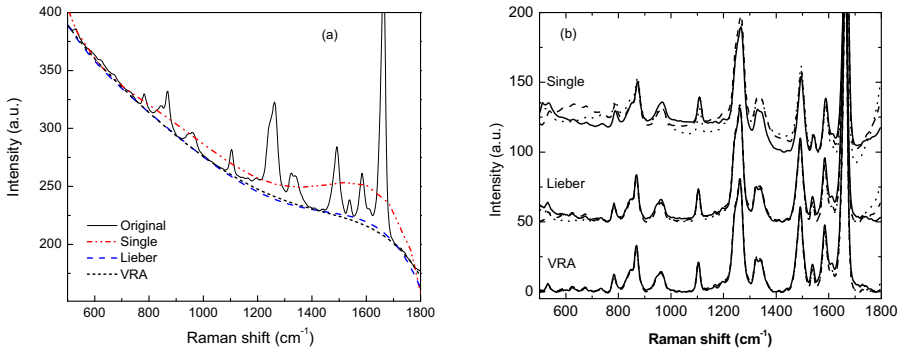

Fig. 6. (a) Raw Raman spectra and the fitted fluorescence background using a fifth order single polynomial (Single), Lieber's modified polynomial (Lieber) and the Vancouver Raman Algorithm (VRA). (b) The final Raman spectra obtained from the three methods with the choice of the fourth-, fifth- and sixth-order polynomial fitting. The sample is solid phase urocanic acid, obtained from Sigma Aldrich, USA without further processing (Adopted from figures 6a and 7 in Zhao *et al.* 2007 with permission).

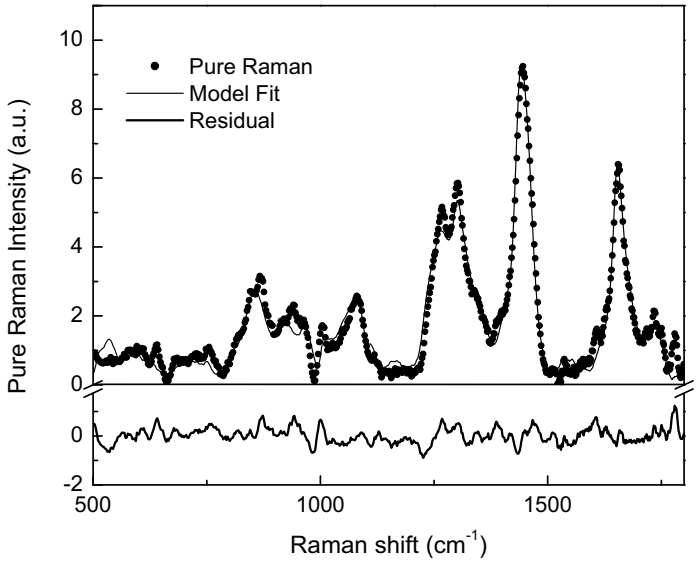

Fig. 7. Modeling of Raman spectra of an Asian volunteer (volar forearm skin) with integration time of 1 second, showing the "pure" Raman spectrum, the general least square fitting, and the fitting residuals for a 5-component reference model (see text) (Adopted from figure 5c in Zhao *et al.* 2008a with permission).

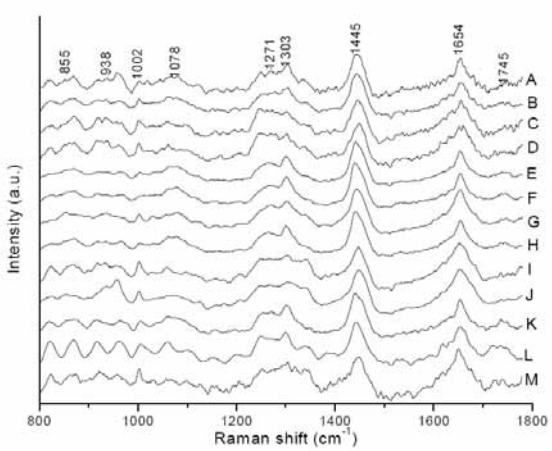

Fig. 8. *In vivo* skin Raman spectra obtained from different skin locations of a healthy volunteer. (A) forehead, (B) cheek, (C) chest, (D) abdomen, (E) volar side of the forearm, (F) surface of the forearm, (G) palm of the hand, (H) dorsal hand, (I) fingertip, (J) fingernail, (K) leg, (L) dorsal foot; (M) sole of the foot (Adopted from figure 2 in Huang *et al.* 2001b with permission).

Peak position (cm^{-1})	Protein Assignment	Lipid Assignment	Others
822 (w)	δ(CCH) aliphatic		
855 (mw)	δ(CCH) aromatic, olefinic		polysaccharide
880 (mw, sh)	ρ(CH_3)		
936 (mw)	ρ(CH_3) terminal, ν(CC) proline, valine		
1002 (mw)	ν(CC) phenyl ring		
1031 (mw)	ν(CC) skeletal		
1065 (mw, sh)		ν_{as}(CC) skeletal	
1080 (ms)		ν(CC) skeletal	ν(CC), $\nu_s(PO_2)$, nucleic acid
1128 (mw, sh)		ν_s(CC) skeletal	
1269 (s, sh)	ν(CN), δ(NH), amide III		
1303 (s, sh)		δ(CH2) twisting, wagging	
1445 (vs)	δ(CH_2), δ(CH_3)	δ(CH_2) scissoring	
1655 (s)	ν(C=O) amide I		
1745 (m)		ν(C=O)	

Table 1. Summary of major Raman bands identified in skin. w: weak, m: medium, s: strong, v: very, sh: shoulder; ν: stretching mode, ν_s: symmetric stretching mode, ν_{as}: asymmetric stretching mode, ρ: rocking mode, δ: bending mode (Adopted from table 1 in Huang *et al.* 2001b with permission).

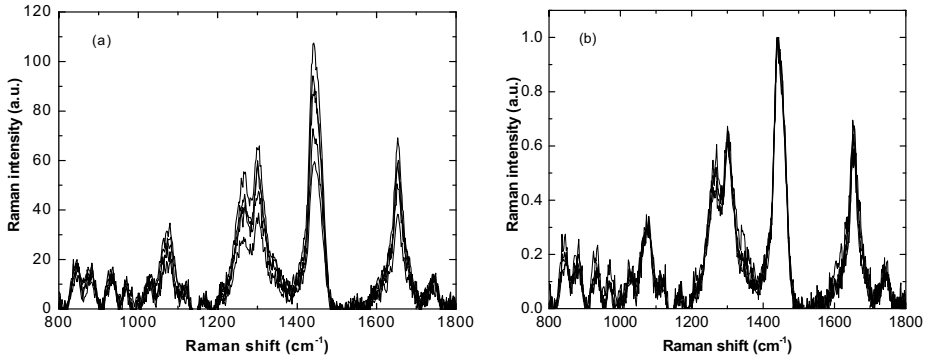

Fig. 9. Sample spectra of human volar forearm skin of 5 subjects showing that the absolute spectra are dramatically different, whereas the normalized spectra have very little variation. (a) absolute Raman spectra, and (b) normalized Raman spectra (Adopted from figure 3 in Zhao *et al.* 2008b with permission).

polynomial fitting and modified polynomial fitting are also presented. Figure 6a is the raw spectra and the fitted fluorescence background of the three methods with the fifth-order polynomial fitting. Note how the intense peak at 1664 cm^{-1} heavily biases the single polynomial fitting. Neither single polynomial fitting method nor Lieber's method generates satisfactory results. Because the peak regions are removed in the Vancouver Raman Algorithm, the bias of the major peaks is minimized. Potential artifacts at both the upper and lower spectral boundary regions are also prevented. Fig. 6b shows the final Raman spectra of the solid phase urocanic acid sample after the fluorescence background removal using the above three methods with the choice of the fourth- (solid line), fifth- (dashed line) and sixth-order (dotted line) polynomial fittings. No method was found to be totally independent of the polynomial order. The Raman spectra from the single polynomial fitting differ significantly for different orders. Lieber's method substantially reduces the variability amongst the choices of orders. The Vancouver Raman Algorithm is the most indifferent with respect to the choice of polynomial order.

Both the Raman spectra and the fluorescence background can be further analyzed. For example, combining the Raman and fluorescence has been shown to improve the sensitivity and specificity of tumor detection (Huang *et al.* 2005). Data analysis models can include reference spectra of morphological and chemical components for general least square fitting, or tissue-specific diagnostic algorithms. Figure 7 shows the Raman spectra, the model fits, and the residuals. In this particular model, the reference Raman spectra of oleic acid, palmitic acid, collagen I, keratin and hemoglobin standard are used. The reference Raman spectra are measured directly from the commercially obtained samples (Sigma Aldrich, St. Luis, MO) without any further processing. The results demonstrated that the skin Raman spectra can be modeled based on these separate components.

4. Applications

The integrated real-time skin Raman system can provide the final Raman spectra in real-time. Its usefulness for *in vivo* skin assessment and skin diseases diagnosis is currently under investigation in our laboratory, and some preliminary results are summarized below.

4.1. *In vivo* Raman spectra of normal skin

We have measured *in vivo* Raman spectra of normal skin on 25 different body sites of 30 healthy volunteers (15 female, 15 male; 17 Caucasian and 13 Asian, average age of 37 years old) (Zhao *et al.* 2008b). Before each measurement, the skin was cleaned with a single wipe of tissue saturated in 70% isopropyl alcohol. The *in vivo* Raman spectra of the skin from different skin regions of the body are shown in Fig. 8. Prominent spectral features in the range of 800-1800 cm^{-1} are the major vibrational bands around 1745, 1655, 1445, 1301, 1269, 1080, 1002, 938, and 855 cm^{-1}. The vibrational assignments for the major skin Raman bands are summarized in Table 1. The strongest band is located at 1445 cm^{-1}, and is assigned to the CH_2 deformations of proteins and lipids. The 1655 cm^{-1} and 1269 cm^{-1} bands are assigned to protein vibrational modes involving in amide I and amide III. The strong band centered at 1301 cm^{-1} is assigned to a twisting deformation of the CH_2 methylene groups of intracellular lipid. The region from 1000 to 1150 cm^{-1} contains information on the hydrocarbon chain. Peaks at 1128 and 1062 cm^{-1} are consistent with C-C stretching modes, while the peak at 1080 cm^{-1} is due to a random conformation vibrational mode. The 1002 cm^{-1} peak, assigned to the phenylalanine breathing mode, is seen in nearly all skin sites, particularly in nail and palm skin.

Distinct Raman peaks in the 800–1800cm^{-1} range can be discerned clearly from various skin sites of the body. We found that within the same subject, skin Raman signals vary significantly according to body sites (Fig. 8). The absolute skin Raman signals for a given body site are also significantly different between subjects, but the normalized Raman spectra (normalized to the strongest peak at 1445 cm^{-1}) have relatively minimal differences as shown in Fig. 9. This may provide unique advantage in skin disease diagnosis. The ratio of the 1655 to 1445 cm^{-1} differs by body site. It shows that keratin-abundant skin sites such as finger-tip and palm regions have the highest mean value (1.023-1.051), and the earlobe the lowest (0.702) (Huang *et al.* 2001b). This means that the lipid/protein compositions are not uniform throughout the body, and this body-site differences need to be factored into skin Raman assessment and disease diagnosis.

4.2. Raman spectra of *in vivo* melanin

Melanin is one of the most ubiquitous and biologically important natural pigments. It is largely responsible for the color of skin, hair, and eyes. Functionally, melanin can act as a sunscreen, scavenge active chemical species, and produce active radicals that can damage DNA. Melanin can be divided into two main classes: a black-to-dark-brown insoluble eumelanin found in black hair and retina of the eye, and a yellow-to-reddish-brown alkali soluble pheomelanin found in red hair and red feathers. Because of its biological importance, particularly its role in skin, melanin has been extensively studied using a wide variety of techniques including mass spectrometry, x-ray diffraction, nuclear magnetic resonance, and scanning tunneling microscopy. Although eumelanin is currently believed to

be a heteropolymer, its chemical structure and biological functions are still subject to debate. Optical measurement is a standard tool for *in vivo* melanin detection and measurement. At the present time, *in vivo* optical measurements of melanin are largely based on its absorption properties. However, melanin has no distinctive absorption peaks to distinguish itself from other cutaneous chromophores such as oxy- and deoxy-hemoglobin, which makes it very difficult to quantify *in vivo*. Raman studies on synthetic melanin and persulfate oxidized tyrosine were carried out by Panina *et al.* (Panina *et al.* 1998) and Cooper *et al.* (Cooper *et al.* 1987). Because the extremely low quantum efficiency of Raman excitation, *in vivo* Raman measurement of melanin has been difficult. We successfully measured for the first the *in vivo* Raman spectra of human skin melanin using the real-time Raman system. Under 785 nm excitation, we have observed two intense and one weak Raman bands from *in vivo* skin and hair as well as from synthetic and natural eumelanins. The three Raman bands are around 1368, 1572 and 1742 cm^{-1}, with subtle differences for different conditions (Huang *et al.* 2004).

In vivo Raman spectra of cutaneous melanin obtained under 785-nm laser excitation are shown in Fig. 10, including dark forearm skin of a volunteer of African descent, a benign compound pigmented nevus, a malignant melanoma, and a normal skin site adjacent to the malignant melanoma. The Raman spectra of normal white skin, dark skin and pigmented lesions are different. Dark skin and pigmented lesions show three intense melanin Raman bands. These three bands can serve as a spectral signature for eumelanin and can potentially be used for noninvasive *in situ* clinical analysis and diagnosis.

4.3. *In vivo* Raman spectra of skin diseases

In vitro Raman spectra of skin diseases and skin cancers have been reported (Gniadecka *et al.* 1997; Gniadecka *et al.* 2003; Gniadecka *et al.* 2004). It was found that for *in vitro* studies, a sensitivity of 85% and a specificity of 99% could be achieved for diagnosis of melanoma (Gniadecka *et al.* 2004). Case studies of *in vivo* Raman spectroscopy of skin cancers are also reported (Huang *et al.* 2001a; Zeng *et al.* 2008; Caspers *et al.* 1998; Caspers *et al.* 2001; Caspers *et al.* 2003; Chrit *et al.* 2005; Gniadecka *et al.* 1997; Gniadecka *et al.* 2003; Gniadecka *et al.* 2004; Lieber *et al.* 2008a; Lieber *et al.* 2008b). Currently we are conducting a large-scale clinical study of skin cancers and skin diseases in order to evaluate the utility of Raman spectroscopy for noninvasive skin cancer detection. We have conducted an intermediate data analysis of 289 cases, of which 24 cases were basal cell carcinoma, 49 cases of squamous cell carcinoma, 37 cases of malignant melanoma, 24 cases of actinic keratosis, 53 cases of seborrheic keratosis, 32 cases of atypical nevus, 22 cases of compound nevus, 25 cases of intradermal nevus, and 23 junctional nevus (Zhao *et al.* 2008c). The normalized mean Raman spectra for different skin cancers and benign skin lesions are shown in Fig. 11. All of them are normalized to the strongest 1445 cm^{-1} peak. Differences in molecular signatures for different skin cancers and skin diseases are apparent. We used partial least squares (PLS) regression of the measured Raman spectra to derive the biochemical constituents in each lesion, and then used linear discriminant analysis (LDA) to classify the skin diseases. Our preliminary results showed that malignant melanoma can be differentiated from other pigmented benign lesions with a diagnostic sensitivity of 97% and specificity of 78%, while precancerous and cancerous lesions can be differentiated from benign lesions with a sensitivity of 91% and specificity of 75%, based on leave-one-out cross-validation (LOO-CV).

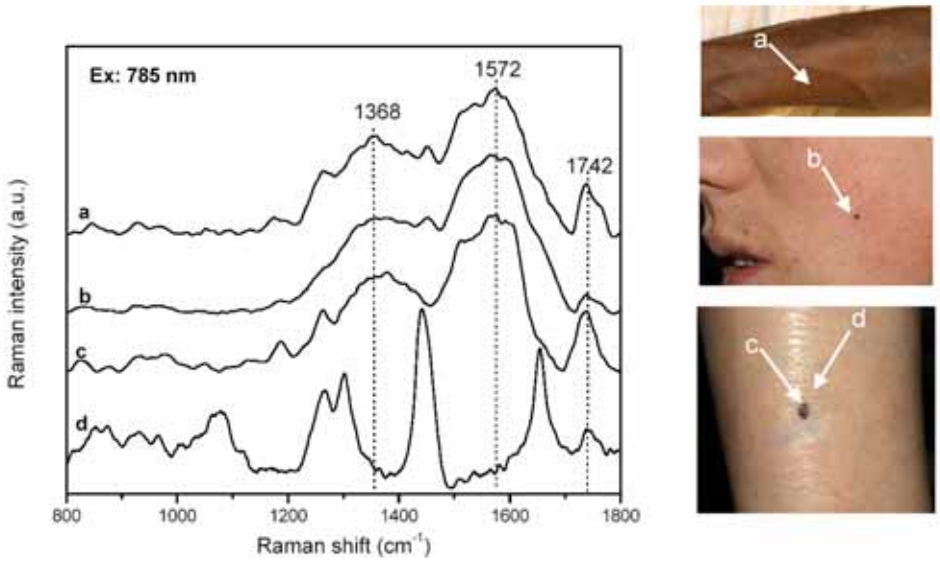

Fig. 10. *In vivo* Raman spectra of cutaneous melanin obtained under 785-nm laser excitation from: (a) volar forearm skin of a volunteer of African descent, (b) benign compound pigmented nevus, (c) malignant melanoma, and (d) normal skin site adjacent to the malignant melanoma. Also shown at the right side are clinical pictures of the corresponding skin sites for *in vivo* Raman measurements (Adopted from figure 7 in Huang *et al.* 2004 with permission).

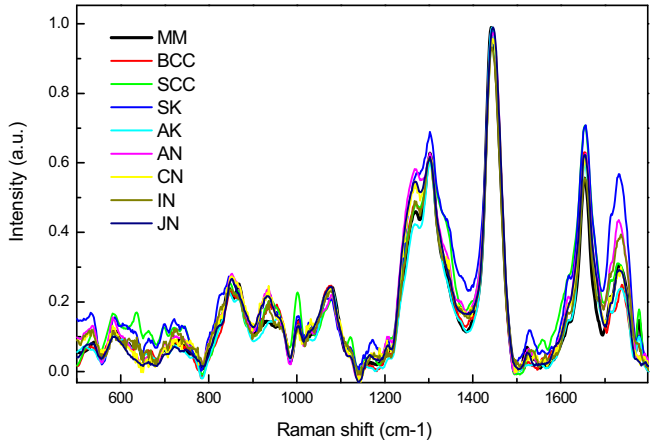

Fig. 11. Normalized Raman spectra of skin cancers and benign skin diseases, including melanoma (MM), basal cell carcinoma (BCC), squamous cell carcinoma (SCC), seborrheic keratosis (SK), actinic keratosis (AK), atypical nevus (AN), compound nevus (CN), intradermal nevus (IN) and junctional nevus (JN) (Adopted from figure 2 in Zhao *et al.* 2008c with permission).

5. Conclusions and future directions

We have developed an integrated real-time Raman spectroscopy system for *in vivo* skin evaluation and skin disease diagnosis. The device includes hardware instrumentation and software implementation. The skin Raman probe maximizes Raman signal collection and minimizes back scattered laser light. It can easily access most body sites. The aberration of the spectrograph image was corrected and the CCD full-chip vertical hardware binning was implemented. Real-time data acquisition and analysis include CCD dark-noise subtraction, wavelength calibration, spectral response calibration, intensity calibration, signal saturation detection and fixing, cosmic ray rejection, fluorescence background removal, and data model analysis. The *in vivo* clinical results validated the utility of the system for potential clinical applications for skin disease diagnosis. Although designed initially for examining the skin, this system can serve as a platform for *in vivo* Raman analysis of tissues from other organs.

We also presented a few examples of real-time *in vivo* Raman spectroscopy for skin. Many potential applications of Raman spectroscopy in skin research remain to be explored. Near future directions include: (1) further clinical trial of real-time Raman spectroscopy as an method for skin cancer and skin disease diagnosis; (2) real-time clinical Raman spectra database management and analysis; (3) Real-time Raman spectroscopy as a method in monitoring cutaneous drugs delivery; (4) Real-time Raman spectroscopy as a method in studying wound healing process; (5) Combination of Raman spectroscopy with confocal microscopy for depth resolved analysis (Wang *et al.* 2009); and (6) Combination of Raman spectroscopy with other imaging methodologies.

6. Acknowledgements

This work is supported by the Canadian Cancer Society, the Canadian Dermatology Foundation, the Canadian Institutes of Health Research, the VGH & UBC Hospital Foundation In It for Life Fund, and the BC Hydro Employees Community Services Fund. We would like to acknowledgment the contributions of our previous group members: Dr. Zhiwei Huang, Dr. Iltefat Hamzavi, Dr. Abdulmajeed Alajlan, Dr. Hana Alkhayat, Dr. Ahmad Al Robaee, and Miss Michelle Zeng. We also thank Mr. Wei Zhang for his technical assistance, and Dr. Michael Chen and Dr. Michael Short for their help.

7. References

Barry B., Edwards H. & Williams A. (1992). Fourier transform Raman and infrared vibrational study of human skin: assignment of spectral bands. *J. Raman Spectrosc.* 23, 641-645, ISSN 0377-0486.

Berger A., Itzkan I. & Feld M. (1997). Feasibility of measuring blood glucose concentration by near-infrared Raman spectroscopy. *Spectrochimica Acta Part A* 53A, 287-292, ISSN 1386-1425.

Caspers P., Lucassen G., Wolthuis R., Bruining H. & Puppels G. (1998). *In vitro* and *in vivo* Raman spectroscopy of human skin. *Biospectroscopy* 4, S31-S39, ISSN 1075-4261.

Caspers P., Lucassen G., Carter E., Bruining H. & Puppels G. (2001). *In vivo* confocal Raman Microspectroscopy of the skin: noninvaisve determination of molecular concentration profiles. *J. Invest. Dermatol.* 116, 434-442, ISSN 0022-202X.

Caspers P., Lucassen G. & Puppels G. (2003). Combined *in vivo* confocal Raman spectroscopy and confocal microscopy of human skin. *Biophys. J.* 85, 572-580, ISSN 0006-3495.

Cheng J. & Xie X. (2004). Coherent anti-Storkes Raman scattering microscopy: instrumentation, theory and applications. *J. Phys. Chem.* B 108, 827-840, ISSN 1520-6106.

Chrit L., Hadjur C., Morel S., Sockalingum G., Lebourdon G., Leroy F. & Manfait M. (2005). *In vivo* chemical investigation of human skin using a confocal Raman fiber optic microprobe. *J. Biomed. Opt.* 10, 44007, ISSN 1083-3668.

Cooper T., Bolton D., Schuschereba S. & Schmeisser E. (1987). Luminescence and Raman spectroscopic characterization of tyrosine oxidized by oersulfate. *Appl. Spectrosc.* 41, 661-667, ISSN 0003-7028.

Edwards H., Williams A. & Barry B. (1995). Potential applications of FT-Raman spectroscopy for dermatological diagnostics. *J. Mol. Struct.* 347, 379-388, ISSN 0166-1280.

Gniadecka M., Wulf H., Mortensen N., Nielsen O. & Christensen D. (1997). Diagnosis of basal cell carcinoma by Raman spectroscopy. *J. Raman Spectrosc.* 28, 125-129, ISSN 0377-0486.

Gniadecka M., Nielsen O., Christensen D. & Wulf H. (1998). Structure of water, proteins, and lipids in intact human skin, hair, and nail. *J. Invest. Dermatol.* 110, 393-398, ISSN 0022-202X.

Gniadecka M., Nielsen O. & Wulf H. (2003). Water content and structure in malignant and benign skin tumours. *J. Mol. Struct.,* 661-662, 405-410, ISSN 0166-1280.

Gniadecka M., Philipsen P., Sigurdsson S., Wessel S., Nielsen O., Christensen D., Hercogova J., Rossen K., Thomsen H., Gniadecki R., Hansen L. & Wulf H. (2004). Melanoma diagnosis by Raman spectroscopy and neural networks: structure alterations in proteins and lipids in intact cancer tissue. *J. Invest. Dermatol.* 122: 443-449, ISSN 0022-202X.

Han X., Lui H., McLean D. & Zeng H. (2009). Near-infrared autofluorescence imaging of cutaneous melanins and human skin *in vivo*. *J. Biomed. Opt.* 14: 024017, ISSN 1083-3668.

Hanlon E., Manoharan R., Koo T., Shafer K., Motz J., Fitzmaurice M., Kramer J., Itzkan I., Dasari R. & Feld M. (2000). Prospects for *in vivo* Raman spectroscopy. *Phys. Med. Biol.* 45: R1-R59, ISSN 0031-9155.

Huang Z., Zeng H., Hamzavi I., McLean D. & Lui H. (2001a). Rapid near-infrared Raman spectroscopy system for real-time *in vivo* skin measurements. *Opt. Lett.* 26: 1782-1784, ISSN 0146-9592.

Huang Z., Zeng H., Hamzavi I., McLean D. & Lui H. (2001b). Evaluation of variations of biomolecular constituents in human skin *in vivo* by near-infrared Raman spectroscopy. *Proceedings of SPIE,* vol. 4597, pp. 109-114.

Huang Z., Lui H., Chen X., Alajlan A., McLean D. & Zeng H. (2004). Raman spectroscopy of *in vivo* cutaneous melanin. *J. Biomed. Opt.* 9, 1198-1205, ISSN 1083-3668.

Huang Z., Lui H., McLean D., Mladen K. & Zeng H. (2005). Raman spectroscopy in combination with background near-infrared autofluorescence enhances the *in vivo* assessment of malignant tissues. *Photochem. Phobiol.* 81, 1219-26, ISSN 0031-8655.

Huang Z., Zeng H., Hamzavi I., Alajlan A., Tan E., McLean D. & Lui H. (2006). Cutaneous melanin exhibits fluorescence emission under near-infrared light excitation. *J. Biomed. Opt.* 11, 034010, ISSN 0146-9592.

Huang Z., Teh S., Zheng W., Mo J., Lin K., Shao X., Ho K., Teh M. & Yeoh K. (2009). Integrated Raman spectroscopy and trimodal wide-field imaging techniques for real-time *in vivo* tissue Raman measurements at endoscopy. *Opt. Lett.* 34, 758-760, ISSN 0146-9692.

Kollias N. & Stamatas G. (2002). Optical non-invasive approaches to diagnosis of skin diseases. *J. Invest. Dermatol. Symposium Proceedings* 7, 64-75.

Lieber C. & Mahadevan-Jansen A. (2003). Automated method for subtraction of fluorescence from biological Raman spectra. *Appl. Spectrosc.* 57, 1363-1367, ISSN 0003-7028.

Lieber C., Majumder S., Billheimer D., Ellis D. & Mahadevan-Jansen A. (2008a). Raman microspectroscopy for skin cancer detection *in vitro*. *J. Biomed. Opt.* 13, 024013, ISSN 1083-3668.

Lieber C., Majumder S., Ellis D., Billheimer D. & Mahadevan-Jansen A. (2008b). *In vivo* nonmelanoma skin cancer diagnosis using Raman microspectroscopy. *Lasers in Surgery and Medicine* 40: 461-467, ISSN 0196-8092.

Mahadevan-Jansen A. & Richards-Kortum R. (1996). Raman spectroscopy for the detection of cancers and precancers. *J. Biomed. Opt.* 1, 31-70, ISSN 1083-3668.

Morris M., Matousek P., Towrie M., Parker A., Goodship A. & Draper E. (2005). Kerr-gated time-resolved Raman spectroscopy of equine cortical bone tissue. *J. Biomed. Opt.* 10, 14014, ISSN 1083-3668.

Motz J., Gandhi S., Scepanovic O., Haka A., Kramer J., Dasari R. & Feld M. (2005a). Real-time Raman system for *in vivo* disease diagnosis. *J. Biomed. Opt.* 10, 031113, ISSN 1083-3668.

Motz J., Hunter M., Galindo L., Gardecki J., Kramer J., Dasari R. & Feld M. (2005b). Optical fiber probe for biomedical Raman spectroscopy. *Appl. Opt.* 43, 542-554, ISSN 0003-6935.

Myrick M., Angels S. & Desiderio R. (1990). Comparison of some fiber optic configurations for measurements of luminescence and Raman scattering. *Appl. Opt.* 29: 1333-13444, ISSN 0003-6935.

Nijssen A., Schut T., Heule F., Caspers P., Hayes D., Neumann M. & Puppels F. (2002). Discriminating basal cell carcinoma from its surrounding tissue by Raman spectroscopy. *J. Invest. Dermatol.* 119, 64-69, ISSN 0022-202X.

Owen H., Battey D., Pelletier M. and Slater J. (1995). New spectroscopic instrument based on volume holographic optical elements. *Proceedings of SPIE,* vol. 2406, 260-267.

Panina L., Kartenko N., Kumzerov Y. and Limonov M. (1998). Comparative study of the spatial organization of biological carbon nanostructures and fullerene-related carbon. *Mol. Mater.* 11, 117-120, ISSN 1058-7276.

Richards-Kortum R. & Sevick-Muraca E. (1996). Quantative optical spectroscopy for tissue diagnosis. *Annu. Rev. Phys. Chem.* 47: 555-606, ISSN 0066-426X.

Santos L., Wolthuis R., Koljenovic S., Almeida R. and Puppels F. (2005). Fiberoptic probes for *in vivo* Raman spectroscopy in the high-wavenumber region. *Anal. Chem.* 77, 6747-6752, ISSN 0003-2700.

Schut T., Wolthuis R., Caspers P. & Puppels G. (2002). Real-time tissue characterization on the basis of *in vivo* Raman spectra. *J. Raman Spectrosc.* 33: 580-585, ISSN 0377-0486.

Shim M. & Wilson B. (1997). Development of an *in vivo* Raman spectroscopic system for diagnostic applications. *J. Raman Spectrosc.* 28, 131-142, ISSN 0377-0486.

Short M., Lui H., McLean D., Zeng H., Alajlan A. & Chen X. (2006). Changes in nuclei and peritumoral collagen within nodular basal cell carcinomas via confocal micro-Raman spectroscopy. *J. Biomed. Opt.* 11: 034004, ISSN 1083-3668.

Short M., Lam S., McWilliams A., Zhao J., Lui H. & Zeng H. (2008). Development and preliminary results of an endoscopic Raman probe for potential *in-vivo* diagnosis of lung cancers. *Opt. Lett.* 33: 711-713, ISSN 0146-9592.

Wang H., Huang N., Zhao J., Lui H., Korbelik M. & Zeng H. (2009). *In vivo* confocal Raman spectroscopy for skin disease diagnosis and characterization - preliminary results from mouse tumor models. *Proceedings of SPIE,* vol. 7161, 716108.

Williams A., Edwards H. & Barry B. (1992). Fourier transform Raman spectroscopy: a novel application for examing human stratum corneum. *Int. J. Pharm.* 81, R11-R14, ISSN 0378-5173.

Zeng H., MacAulay C., McLean D. & Palcic B. (1995). Spectroscopic and microscopic characteristics of human skin autofluorescence emission. *Photochem. Phobiol.* 61: 639-645, ISSN 0031-8655.

Zeng H., MacAulay C., McLean D., Palcic B. & Lui H. (1998). The dynamics of laser-induced changes in human skin autofluorescence - experimental measurements and theoretical modeling. *Photochem. Phobiol.* 68: 227-236, ISSN 0031-8655.

Zeng H. (2002). Apparatus and methods relating to high speed Raman spectroscopy. United States Patent #: 6486948.

Zeng H., Zhao J., Short M., McLean D., Lam S., McWilliams A. & Lui H. (2008). Raman spectroscopy for *in vivo* tissue analysis and diagnosis, from instrument development to clinical applications. *J. Innovative Optical Health Sciences,* 1, 95-106, ISSN 1793-5458.

Zhao J., Lui H., McLean D. & Zeng H. (2007). Automated Autofluorescence Background Subtraction Algorithm for Biomedical Raman Spectroscopy. *Appl. Spectrosc.* 61, 1225-1232, ISSN 0003-7028.

Zhao J., Lui H., McLean D. & Zeng H. (2008a). Integrated real-time Raman system for clinical *in vivo* skin analysis. *Skin Res. and Tech.* 14, 484-492, ISSN 0909-752X.

Zhao J., Huang Z., Zeng H., McLean D. & Lui H. (2008b). Quantitative analysis of skin chemicals using rapid near-infrared Raman spectroscopy. *Proceedings of SPIE*, vol. 6842, 684209.

Zhao J., Lui H., McLean D. & Zeng H. (2008c). Real-time Raman spectroscopy for non-invasive skin cancer detection - preliminary results. *Proceedings of the 30th Annual International Conference of the IEEE Engineering in Medicine and Biology Society*, pp. 3107-3109, ISBN 978-1-4244-1815-2, Vancouver, British Columbia, Canada, August 20-24, 2008.